Nickel Structures as a Template-Strategy to Create Shaped Iridium Electrocatalysts for Electrochemical Water Splitting

Seongeun Park,[1,‡] Meital Shviro,[1,‡,*] Heinrich Hartmann,[2] Astrid Besmehn,[2] Joachim Mayer,[3,4] Detlef Stolten[5,6] and Marcelo Carmo[1,7]

[1] Institute of Energy and Climate Research, Electrochemical Process Engineering (IEK-14) Forschungszentrum Jülich GmbH, 52425 Jülich, Germany

[2] Central Institute for Engineering, Electronics and Analytics (ZEA-3) Forschungszentrum Jülich GmbH, 52425 Jülich, Germany

[3] ER-C 2, Forschungszentrum Jülich GmbH, 52425 Jülich, Germany

[4] GFE, RWTH Aachen University, 52074 Aachen, Germany

[5] Institute of Energy and Climate Research, Techno-economic Systems Analysis (IEK-3) Forschungszentrum Jülich GmbH, 52425 Jülich, Germany

[6] Chair for Fuel Cells, RWTH Aachen University, Germany

[7] Mechanical and Materials Engineering, Queen's University, Kingston, ON, K7L 3N6, Canada

[‡] These authors contributed equally.

* Corresponding Author: m.shviro@fz-juelich.de

ABSTRACT: Low-cost, highly active, and highly stable catalysts desired for the generation of hydrogen and oxygen using water electrolyzers. To enhance the kinetics of the oxygen evolution reaction in an acidic medium, it is of paramount importance to re-design iridium electrocatalysts into novel structures with organized morphology and high surface area. Here we report on the designing of a well-defined and highly active hollow nanoframe based on iridium. The synthesis strategy was to control the shape of nickel nanostructures on which iridium nanoparticles will grow. After the growth of iridium on the surface, the next step was to etch the nickel core to form the NiIr hollow nanoframe. The etching procedure was found to be significant in controlling the hydroxide species on the iridium surface and by that affecting the performance. The catalytic performance of the NiIr hollow nanoframe was studied for oxygen evolution reaction and shows 29 times increased iridium mass activity compared to commercially available iridium based catalysts. Our study provides novel insights to control the fabrication of iridium-shaped catalysts using 3d transition metal as a template, and via facile etching step to steer the formation of hydroxide species on the surface. These findings shall aid the community to finally create stable iridium alloys for polymer electrolyte membrane water electrolyzers, and the strategy is also useful for many other electrochemical devices such as batteries, fuel cells, sensors, and solar organic cells.

Keywords: Iridium, structural-evolution, hollow nanoframe, nanoarchitectures, oxygen evolution reaction, electrocatalysis

Table of Contents

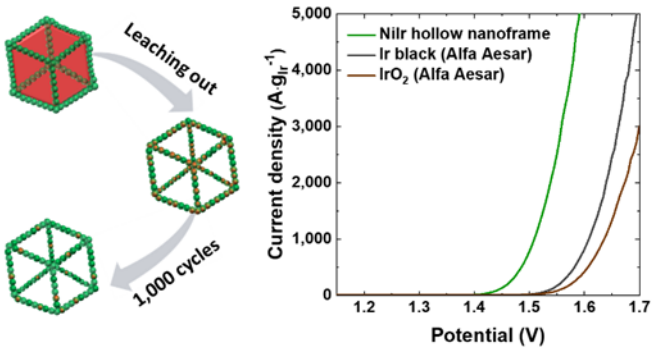

INTRODUCTION

Out of the different water electrolysis technologies, polymer electrolyte membrane (PEM) water electrolyzers are currently of great interest as it provides numerous advantages in contrast to alkaline electrolyzers, such as wide load range, high efficiency, and compact system design, etc.[1,2] However, the acidic working environment at the cell level restricts the use of electrocatalysts to a handful of options based on less abundant iridium and platinum elements.[1,2]

There have been extensive research initiatives attempting to develop cost-efficient electrocatalysts that can be used in various electrochemical energy storage and conversion devices such as fuel cells[3], batteries[4], and photocatalytic conversion reactors[5,6]. For PEM water electrolyzers, much fewer catalysts alternatives that can replace or at least effectively reduce the amount of iridium exist. To date, RuO_2 and IrO_2 have still shown the highest activity for the oxygen evolution reaction in acidic media, but RuO_2 is far less stable than IrO_2 as it undergoes strong dissolution over time.[7–10] For this reason, IrO_2 is still regarded as the benchmark catalyst for oxygen evolution in acidic conditions.[11–20] Besides, not many publications were found to report a significant reduction of the noble metal amount and simultaneously boosting the electrocatalytic performance of iridium catalysts.[21–25] One route is the fabrication of hollow nanostructures[26–31] that allows a much larger surface area available for the reaction compared to conventional nanoparticles.[32–34] These hollow structures are thought to facilitate ion movement towards the electrolyte promoting reaction kinetics. Many hollow nanostructures ranging from 1D to 3D have been introduced, but not much effort has been made to design hollow structures based on iridium that is expected to exhibit high catalytic activity. Park et al. showed that iridium-based multimetallic nanoframes have higher electrocatalytic performance compared to Ir/C with additional information that the double-walled frame structure showed improved performance than the single-walled frame structure.[35] Another approach was done by alloying iridium with transition metals followed by metal etching, de-alloying, or metal displacement procedures.[36,37] Transition metals are frequently used to fabricate hollow nanostructures due to their advantageous properties that can be effectively etched or replaced in the structures. The abundant reserves and low prices of transition metals are also attractive from an economic point of view. Moreover, improved electrocatalytic activity, known as ‘d-band engineering’ can be expected.[38] Transition metals can induce a

slight shift in the d-band center, which tunes the balance between the binding and adsorption energy that enhances the catalytic activity.[38,39] Xue et al. reported that graphdiyne anchored with a single nickel or iron atom exhibited greatly enhanced catalytic performance for hydrogen evolution reaction compared to bare graphdiyne or commercial Pt/C, and explained the synergistic effect by anchoring nickel or iron atoms through a theoretical study.[39] Amongst the transition metals, nickel is a preferable material to alloy with iridium as it allows to control of the synthesis process and catalyst engineering. Lim et al. reported several morphologies of Ir-Ni nanostructures by tuning the ratio of the precursors.[40] All the bimetallic Ir-Ni nanostructures showed higher current density than iridium supported on carbon. Wang et al. investigated 132 couplings for alloy nanoparticles, which gave insight into the optimal design of core-shell nanostructures.[41] The combination of iridium and nickel leads to the formation of core-shell structures; however, progression to a binary alloy phase cannot be achieved, given the lattice mismatch between the two metals, meaning that the reaction between the two elements will be mostly separated into two parts. Besides, nickel has been reported as being more effective to obtain "d-band engineering" with iridium than other metals.[42] Since nickel is superior to generate hole-doped sites while it is leached out from the structure, it leads iridium-based nanostructures to be more catalytically active and highly stable. Nong et al. proved that the $IrNiO_x$ nanoparticles are more favorable for electrocatalytic performance than other iridium-based materials reported in the literature supported by density functional theory calculation.[42] This finding regarding the beneficial synergic between iridium and nickel was also confirmed by Reier et al., which showed that an Ir-Ni mixed oxide structure exhibits higher oxygen evolution reaction activity compared to iridium alone. Ir-OH species formed while nickel is dissolved in the electrolyte and lead to the formation of a highly active surface.[43]

Here we fabricated NiIr hollow nanoframes, using a holistic approach as our starting point, investigating the synthesis, structure, catalytic activity, and stability for the oxygen evolution reaction. Since controlling the shape of iridium nanostructures is far from simple, the concept here was to use nickel as a template. Several strategies are known to shape nickel nanoparticles, and we chose a surfactant-assisted solvothermal reaction. The hexagonal structure that has a nickel core and iridium decoration on the surface was formed as the initial structure successfully achieved by using a long amine chain act as not only a surfactant and solvent but also as a reduction agent. As the next step, the hollow nanoframe formed from the NiIr hexagonal structure by selectively etching the leachable component and was evaluated as an electrocatalyst for the oxygen evolution reaction. The NiIr hollow nanoframe showed highly superior activity by comparison with commonly used commercial iridium catalysts.

RESULTS AND DISCUSSION

Structural characterization

Uniform NiIr hexagonal nanostructures were synthesized through a surfactant-assisted process. In brief, the nanostructures were synthesized in oleylamine (OA) that functions as the reducing and capping agent. The iridium

precursor was reduced when nickel nanoparticle was already formed and verified using the same experimental conditions; without the use of nickel, iridium nanoparticles cannot be created (Figure S1A, B). From this, we can infer that nickel nanoparticles formed first and followed by the growth of iridium nanoparticles. While the synthesis was performed without iridium precursor, the irregular shape of nickel nanoparticles occurred (Figure S1C, D). To achieve the desired nanostructure, the reaction was carried out at a temperature above 200 °C to deposit the iridium nanoparticles on the nickel surface. Figure 1 presents a high angle annular dark-field (HAADF) scanning transmission electron microscopy (STEM) images of the NiIr nanostructures. It shows a hexagonal nanostructure shape that is 42 ± 5 nm in size (Figure 1A). Figure 1B shows the enlarged, high-resolution HAADF-STEM image and Fourier transformation (FFT) pattern of the green area in Figure 1A, where the iridium face-centered cubic (FCC) structure confirmed at the vertex of the shell. In the line scans along the NiIr hexagonal nanostructure (Figure 1C), it is indicated that the inner bulk consists of nickel with a symmetrical profile, and the iridium is distributed mainly on the edges and vertices. The elemental distribution of NiIr hexagonal nanostructure was verified by energy-dispersive X-ray (EDX) elemental mapping (Figure 1D-F), which exhibits that iridium atoms deposited on the nickel surface, especially along the edges that are more chemically active than the facets.[44,45] The atomic composition measured by the EDX of NiIr hexagonal nanostructure was set to Ni 97 at% and Ir 3 at%.

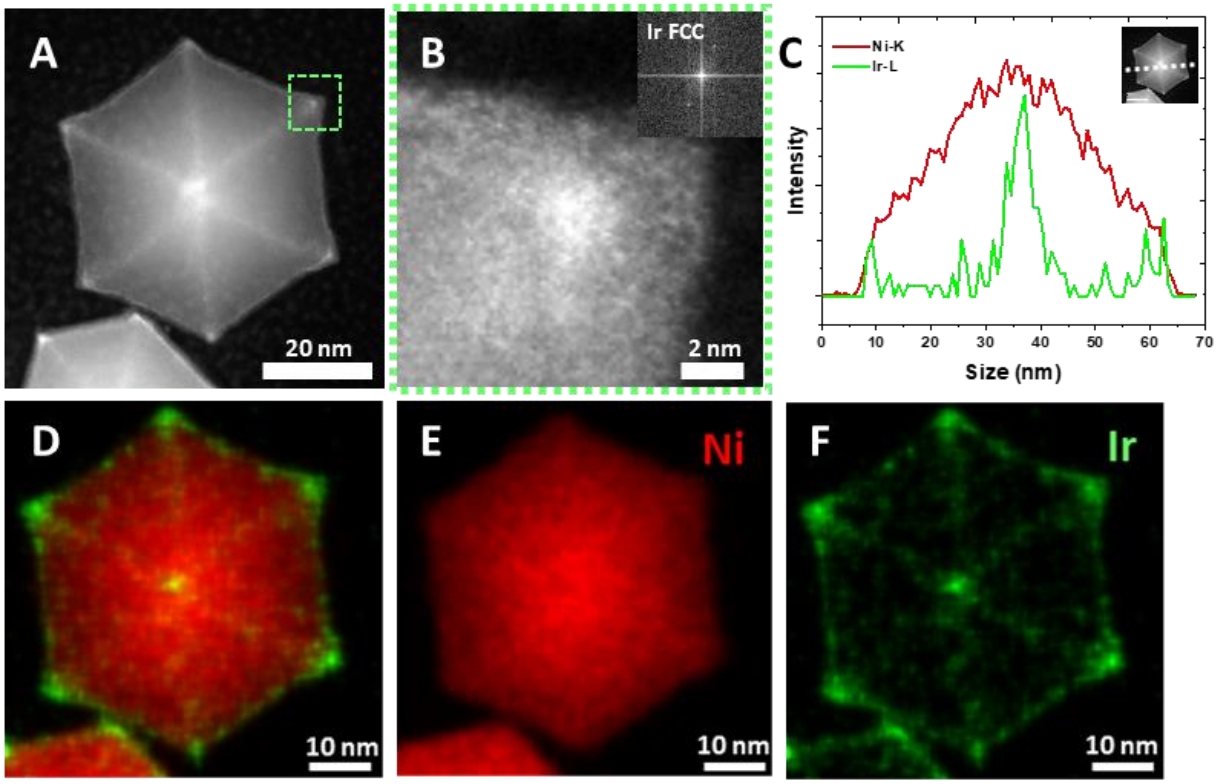

Figure 1. Morphology and composition profile analysis of the pristine-NiIr hexagonal nanostructure. (A) HAADF-STEM image; (B) magnified view of the selected green area with high-resolution HAADF-STEM and FFT pattern;

(C) line scan analysis of NiIr hexagonal nanostructure along the white dash line of inset; and (D-F) distribution of Ni (red) and Ir (green) across the EDX composition maps.

To understand the growth mechanism of iridium on nickel, we explored the effect of the reaction time on particle growth (Figure 2), studying the formation process by analyzing TEM images at several reaction stages. At the initial stage, following a 10 min reaction, nickel nanoparticles of approximately 20 nm in size were formed (Figure 2A). From the FFT pattern (Figure S2A), (111) and (200) nickel reflections were confirmed to exhibit the FCC structure. Small iridium nanoparticles also began to form and are located between the nickel nanoparticles (Figure 2A). After 30 min reaction time, the hexagonal structure of nickel nanoparticles emerged. It displays clear and thin outer shells, as well as a uniform size distribution (Figure 2B, S2B). At the same time, the iridium nanoparticles are rarely discovered, which suggests that the small iridium nanoparticles used to form the outer shell of the NiIr hexagonal nanostructures during the reaction, as shown in Figure 1. When extending the reaction time for more than 60 min, the nickel nanoparticles grow and form irregular shapes (Figure 2C, Figure S2C). The iridium nanoparticles which grow on top of the nickel surface will not continue to form a thick shell, but instead will nucleate and grow to form small iridium nanoparticles (Figure S3). As estimated by Xia et al., the energy barrier for the homogenous nucleation of iridium is smaller than the energy needed for heterogeneous nucleation. In the catalyst system discussed here, the energy barrier for further deposits of iridium atoms is higher than the energy needed for the self-nucleation of iridium.[46] This indicates that iridium atoms prefer to grow in small nanoparticles and form more iridium nuclei instead of being overgrown into large iridium nanoparticles. In our growth study, this estimation perfectly fits the aspect of nanoparticle growth. While the reaction increases to 60 min, the number of iridium nanoparticles surrounding the nickel surface increases dramatically (Figure 2C). The EDX elemental distribution supports and highlights this more clearly (Figure S3).

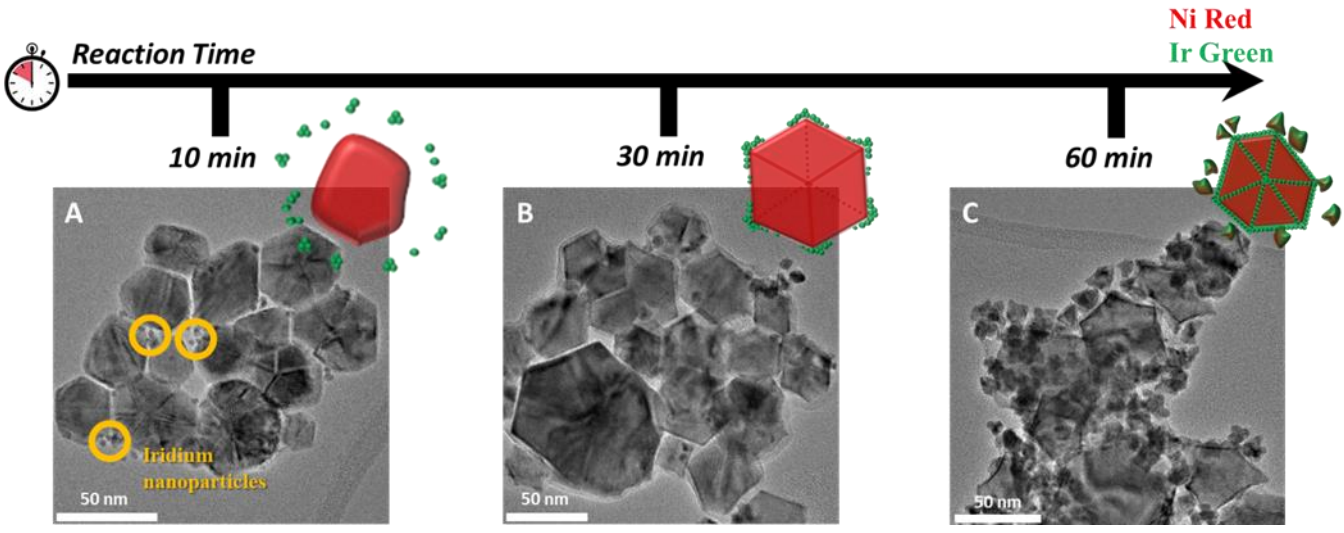

Figure 2. Growth study of NiIr hexagonal nanostructures. Bright-field TEM images and nanoparticle illustration of the reaction products at (A) 10 min; (B) 30 min; (C) 60 min. Iridium atoms prefer to grow in small nanoparticles and

form more iridium nuclei instead of being overgrown into large iridium nanoparticles. When the reaction increases to 60 min, the number of iridium nanoparticles surrounding the nickel surface increases dramatically.

The next step was to leach out part of the nickel to form the hollow structure. HCl 4 mol·L^{-1} was used to leach nickel from the structure, but also to favor the diffusion of iridium inside via the 'Kirkendall effect'.[28,47,48] When the nickel atoms etched, vacancies were generated and utilized as paths for the migration of iridium. Iridium moved along the vacancies and formed a well-mixed frame with the remaining nickel. Figure 3 and Figure S6A shows the NiIr hollow nanoframe formed after leaching. The hollow frame retains the original structure (Figure 3A), and the line scan profile (along with the white dash line in Figure 3A) confirms the leaching of the inner nickel and the formation of a rich-iridium frame. The corresponding EDX elemental mappings (Figure 3B-D) further pointed out that nickel and iridium were distributed, with the nanostructure consisting of 28 at% of Ni and 72 at% of Ir.

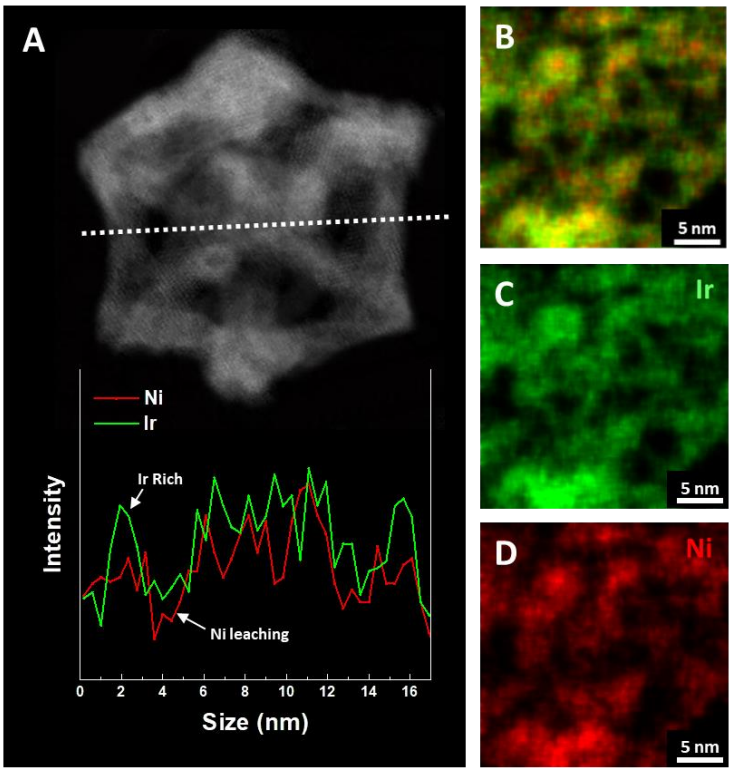

Figure 3. Morphology and composition profile analysis of the NiIr hollow nanoframes. (A) A high-resolution HAADF-STEM image of NiIr hollow nanoframe and a line scan profile along the white dash line; (B-D) the distribution of Ir (green) and Ni (red) in the EDX composition maps. The hollow frame retains the original structure and the line scan profile (along with the white dash line in Figure 3A) confirms the leaching of the inner nickel and the formation of a rich- iridium frame.

The transformation of the NiIr nanostructure before and after the leaching step was analyzed by X-ray diffractions (XRD). The red, orange, green, and light green lines at the bottom represent the diffraction patterns of Ni, NiO, Ir,

and IrO_2 standards, respectively. The NiIr hexagonal nanostructure shows the presence of Ni (111), (200), (220), and (311) peaks indicating the Ni FCC structure (JCPDS 06-0598) and supporting the morphological characterizations in Figure 1. Iridium forms a thin layer on the nickel nanostructure and cannot distinguish in the XRD pattern. After the leaching process, the XRD pattern shows the shift of diffraction peaks to lower angles, indicating the formation of iridium-based FCC (JCPDS 06-0598) nanoframe structure.

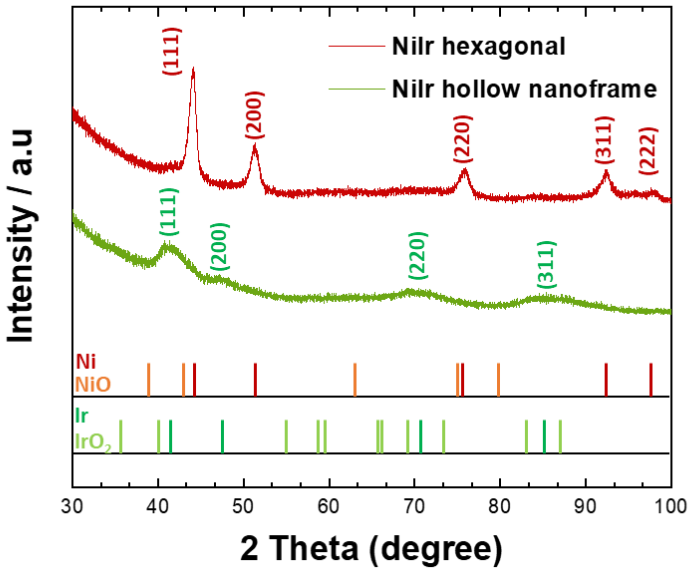

Figure 4. X-ray diffraction patterns of NiIr hexagonal nanostructures (before leaching) and NiIr hollow nanoframes (after leaching).

X-ray photoelectron spectroscopy (XPS) was used to determine the specific oxidation and chemical state of the NiIr hexagonal nanostructures and NiIr hollow nanoframes. Measurements of the nickel 2p and iridium 4f regions were performed to determine the presence and to qualitatively compare the relative contribution of metallic and oxide surface species based on prior studies.[49–52] Figure 5 shows the X-ray photoelectron spectra in the Ir 4f/Ni 3p, Ni $2p_{3/2}$, and O 1s spectral regions. The peaks in the Ir 4f region of NiIr hexagonal nanostructures and NiIr hollow nanoframes show the presence of peaks with the binding energies that are consistent with metallic iridium (Figure 5A). The XPS spectra of NiIr hexagonal nanostructures within the Ni $2p_{3/2}$ region (Figure 5B) depicts metallic and Ni^{3+} components with an almost 1:1 ratio. Those findings were also confirmed by the fitting of the Ni 3p region which is overlapped in the Ir 4f signal. After etching, the nickel spectrum in the Ni $2p_{3/2}$ region still consists of the same two components but with a considerable decrease of the oxidized fraction, and the peaks of the Ni 3p region vanished. It explains that the unstable nickel that existed in the structure was leached out, and the remained nickel has mostly a metallic surface property. Figure 5C shows the peaks in the O 1s region which are related to nickel oxide, iridium hydroxide, and water

(marked as Ni-O, Ir-OH, Ir-OH_2). Comparing with NiIr hexagonal nanostructure, it is confirmed that the Ni-O peak was remarkably weakened from 14.0 at% to 2.7 at% and the Ir-OH peak became more intense for NiIr hollow nanoframe as 83.2 at% than before (71.4 at%), which originated from the leaching step. On the contrary, the peak indicating Ir-OH_2 showed no remarkable difference, 14.6 at% to 14.1 at%, which means the loss of Ni-O mostly contributed to the increase of Ir-OH species on the surface. When nickel leached out in the acidic solution, the oxygen atoms lose their binding partner. This leads to the connection with a proton from the electrolyte to form the hydroxyl group, as previously suggested and reported as one of the reasons for more efficient oxygen evolution.[43,53–55] Overall, the XPS data supports that the surface region of NiIr hollow nanoframes contains metallic iridium and metallic nickel as well as a contribution from Ir-OH in the surface.

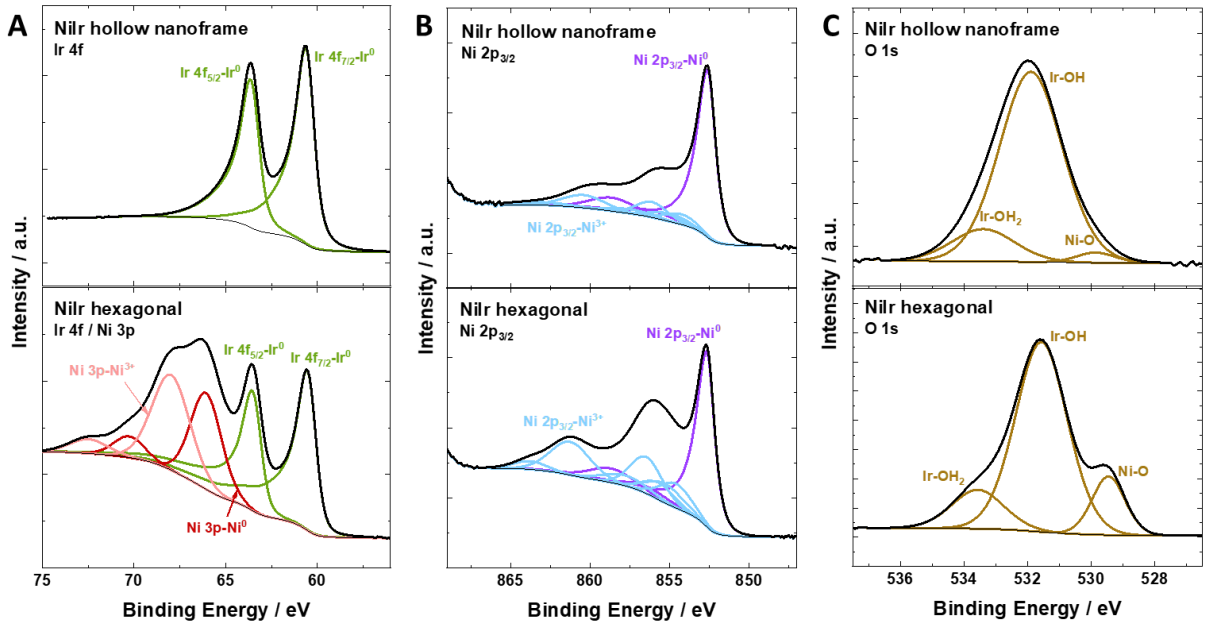

Figure 5. X-ray photoelectron spectra of NiIr hexagonal nanostructures and NiIr hollow nanoframes in the (A) Ir 4f/Ni 3p, (B) Ni $2p_{3/2,}$ (C) O 1s regions. When nickel leached out in the acidic solution, the oxygen atoms lose their binding partner. This leads to the connection with a proton from the electrolyte to form the hydroxyl group, as one of the reasons for more efficient oxygen evolution.

Our observations regarding the formation of the NiIr hollow nanoframes are illustrated in Figure 6. The development of the morphological process proposed here could extend to incorporate the synthesis of iridium shells with other shapes and facets through the use of nickel nanostructures. The morphological evolution series begins with an irregular nickel shape surrounded by small iridium nanoparticles (Figure 6A). With longer reaction time, iridium nanoparticles gather and attach along the edges of the nickel nanostructure to form a NiIr hexagonal nanostructure (Figure 6B, C). Through the leaching procedure, the nanostructure loses the inner component of nickel, which leads to the formation

of a hollow nanoframe structure consisting of nickel and iridium (Figure 6D). Figure 6E shows how the alloy of the outer shell formed during the acid leaching procedure. According to the generated vacancies, the iridium atoms diffuse inward, followed by the formation of a well-mixed alloy shell.

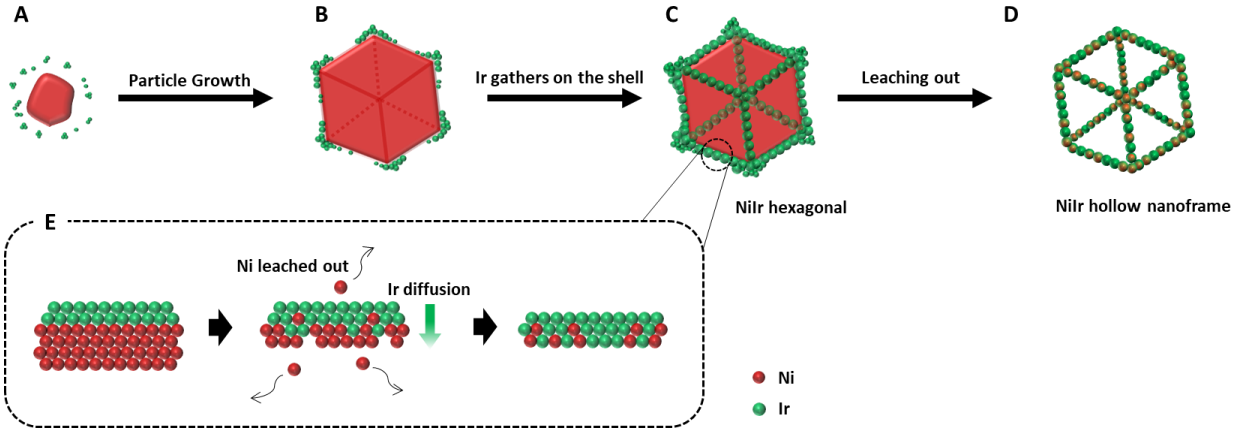

Figure 6. Schematic illustration of the formation of the NiIr hollow nanoframe. (A-C) Formation of the NiIr hexagonal nanostructure; (D) the NiIr hollow nanoframe after the leaching out step; and (E) the enlarged description of the edge area during the leaching step.

3.2 Electrochemical measurements

The electrocatalytic performance for oxygen evolution of NiIr hollow nanoframes was carried out and compared to commercial Ir-black and IrO_2 from Alfa Aesar (Figure 7). Figure 7A displays the linear sweep voltammetry (LSV) curves of NiIr hollow nanoframes and both commercial catalysts. The NiIr hollow nanoframes demonstrated higher activity than Ir-black and IrO_2. To drive 10 $mA \cdot cm^{-2}$, NiIr hollow nanoframes requested 269 mV of overpotential while the commercial Ir-black and IrO_2 needed 354 mV, and 396 mV, respectively. At 1.51 V, the estimated average-mass activity was 887 $A \cdot g_{Ir}^{-1}$ for the NiIr hollow nanoframes and 30 $A \cdot g_{Ir}^{-1}$ for Ir-black, and 16 $A \cdot g_{Ir}^{-1}$ for IrO_2 (Figure 7C, Figure S4). The NiIr hollow nanoframes showed a 29 fold improved mass activity than the Ir-black and IrO_2. When comparing with the literature (Table S1), our NiIr hollow nanoframes also showed significantly higher mass activity. Lim et al. reported 498 $A \cdot g_{Ir}^{-1}$ for Ir-Ni thin layers (1.51 V)[40] and Nong et al. reported 583 $A \cdot g_{Ir}^{-1}$ (1.53 V) while using IrNi@IrO_x core-shell nanoparticles.[56] This remarkably improved performance from a here proposed advantage that NiIr hollow nanoframes possess. The NiIr hollow nanoframe is more beneficial to achieve higher mass activity than solid iridium particles by reducing the inside part which cannot be participated in the electrocatalytic reaction.[57] As shown in the STEM images, the NiIr hollow nanoframe exposed the iridium on the surface efficiently increasing the catalyst utilization.[58–60] As previously reported by Ren et al., palladium hollow nanocrystal was compared to Ni@Pd and solid Pd particles as electrocatalysts for formic acid oxidation, and exhibited higher activity than the others.[58] Wang et al. introduced Pt icosahedral nanocages showing highly improved mass activity than the

commercial Pt/C catalysts for oxygen reduction reaction.[59] Besides, the NiIr hollow nanoframe has FCC structure with (111) facets which was confirmed by the XRD pattern. The (111) facet has been reported as the most preferred for electrocatalysts in general because of the higher atomic packing density and lower surface energy that attribute to a higher catalytic activity.[61,62] Furthermore, the NiIr hollow nanoframe has an advantageous surface property with iridium and nickel metallic species, and Ir-OH species on the surface. In particular, the presence of the Ir-OH species on the surface plays a crucial role in the enhancement of the oxygen evolution reaction.[55,63] The Ir-OH species are known to be generated during the leaching of nickel. When the nickel is leached out, the oxygen atom that lost nickel but held by iridium remains, and the atom catches proton in the electrolyte, which forms Ir-OH species. Godínez-Salomón et al. reported that the interaction with nickel on the iridium surface decreases the activation energy of the second electron transfer step for oxygen evolution reaction that is known as the rate-determining step via density functional theory calculation.[55] As supported by the XPS results in our study, it demonstrates that the decrease of Ni-O peak and the increase in Ir-OH species on the surface can be achieved after the chemically leaching procedure, and it contributes to the enhancement of electrocatalytic activity (Figure 5).

An aging test protocol was conducted by cycling the catalyst from 1.1 V to 1.6 V at 100 $mV \cdot s^{-1}$ for one thousand times to evaluate the stability of the NiIr hollow nanoframes. As a result, the overpotential of the NiIr hollow nanoframes increased by 13 %, whereas Ir-black and IrO_2 showed 5 % and 6 % degradation. Nevertheless, the NiIr hollow nanoframes still showed an overall lower overpotential than both iridium commercial catalysts after one thousand cycles (Figure 7B). Next, we analyzed the kinetics of the catalysts based on their Tafel slopes for the oxygen evolution reaction. Before the durability test, the Tafel slopes for all samples were in the range of 60 $mV \cdot dec^{-1}$, indicating that the switching step of the surface adsorbed "-OH" groups from physical adsorption to chemical adsorption is the rate-determining step.[64–66] After the durability test, the slopes did not deteriorate significantly, increasing from 56.4 mV·dec-1 to 63.5 $mV \cdot dec^{-1}$ and from 64.5 $mV \cdot dec^{-1}$ to 73.9 mV·dec-1 for Ir-black and IrO_2, respectively. In contrast, the NiIr hollow nanoframes showed an opposite trend that their Tafel slopes even slightly decreased from 61.3 $mV \cdot dec^{-1}$ to 55.7 $mV \cdot dec^{-1}$ after the aging test. It is suggested that the effect of nickel leaching during the electrochemical test leads to the formation of an additional hydroxyl group on the surface and may contribute to the kinetics. To study the structural stability of the NiIr hollow nanoframes, we conducted the morphological characterization of the hollow nanoframes after the durability test (Figure 7D, E, Figure S6B). Elemental EDX mapping was conducted and the nickel concentration was found to be less than 3 at% (Figure 7E). These results indicate that nickel atoms migrated to the surface of the nanostructure and dissolved in the solution. To evaluate possible electrochemical leaching of nickel during the durability test, we performed inductively coupled plasma mass spectrometry (ICP-MS) with the electrolyte samples after the durability test. As a result, 0.9 wt% of iridium and 18.0 wt% of nickel which was coated onto the electrode were detected within the electrolyte. This may explain the degradation of NiIr hollow nanoframes since the electrochemically leached nickel in the electrolyte can impede the electrochemical reaction by increasing the losses. However, NiIr hollow nanoframes showed lower overpotential compared to Ir-black and IrO_2 (IrNi hollow nanoframe 303 mV, Ir-black 371 mV, IrO_2

419 mV). We speculate that the electrochemically leached nickel contributed to the generation of more Ir-OH species on the surface, which will be linked to the improved electrocatalytic activity. Moreover, the catalyst structure has been maintained without collapse, which will retain the life span of electrocatalysts by avoiding the agglomeration that can be caused by destroyed particles, and it can be explained by the bimetallic effect on the stability of materials which has been already reported.[62,67–69] Huang et al. showed that the Pd-Ni bimetallic nanoparticles have improved structural and thermodynamic stability than monometallic nickel or palladium nanoparticles through the computational method with supporting experiments.[67] Beermann et al. reported that surface doping can be strongly effective to stabilize catalyst nanostructures.[62] Rh doping on the surface of PtNi octahedral nanoparticles efficiently suppressed the migration of Pt atoms at the edges and results in the prevention of the shape loss. Based on prior research, it is interpreted that the remaining nickel is working in the structure for the catalyst's robustness.

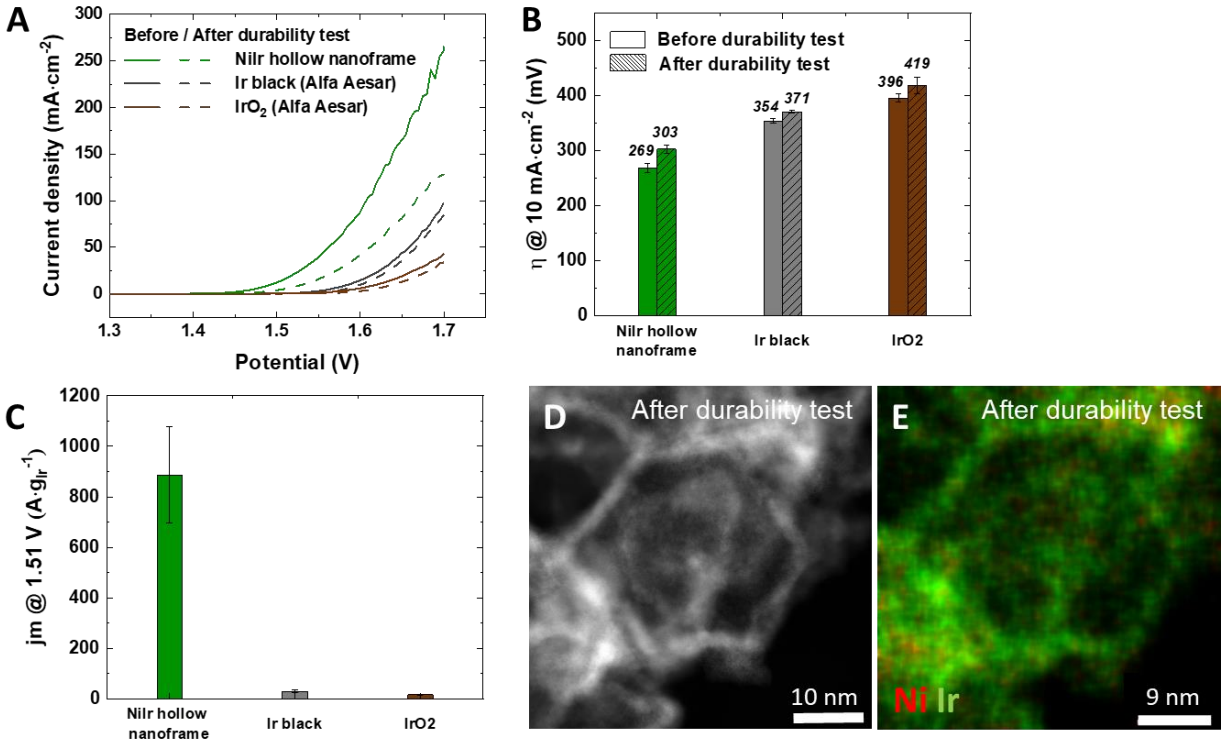

Figure 7. Electrocatalytic activity of the NiIr hollow nanoframes by comparison with commercial Ir-black and IrO_2. (A) LSV curves of the NiIr hollow structures and commercial Ir-black and IrO_2 measured in 0.5 M H_2SO_4 before and after the aging test of 1,000 cycles from 1.1 V to 1.6 V; (B) bar graph displaying the overpotentials to drive 10 $mA \cdot cm^{-2}$; (C) Ir mass activities at 1.51 V (vs. RHE); (D) HAADF-STEM image of the NiIr hollow nanoframe after 1,000 cycles; and (E) distribution of the Ni (red) and Ir (green) in the EDX composition maps.

CONCLUSIONS

In this study, morphology and structure controlled nickel was used as a strategy to steer the shape of iridium based electrocatalysts for water electrolysis. We synthesized NiIr hexagonal nanostructures as the base material followed by chemical leaching to form the NiIr hollow nanoframes. The growth mechanism was studied and reveals that the difference in the kinetic growth of two elements leads to the formation of nickel structure followed by the growth of iridium nanoparticles on the surface of the nickel. Since the growth rates of iridium and nickel are different, the outcomes can be different depends on the reaction time, therefore the reaction time can be sensitively controlled to achieve the desired structure. After the leaching of nickel core from the structure, the successful fabrication of NiIr hollow nanoframes was achieved. The NiIr hollow nanoframes were tested as electrocatalysts for the oxygen evolution reaction in an acidic electrolyte and showed enhanced electrocatalytic activity (269 mV at 10 $mA \cdot cm^{-2}$) and mass activity (887 $A \cdot gIr^{-1}$) compared to commercial Ir-black and IrO_2. The improved electrocatalytic performance was attributed to the well-defined FCC structure which exposes active metallic iridium (111) facets and the interaction on the surface between nickel and iridium which increases the concentration of Ir-OH on the surface during the leaching of nickel. Considering the effect of the additional element on the improved stability of the structure, bimetallic nanostructures including transition metals can be an economic strategy to efficiently utilize noble metals. This study will give important insights into the designing of bimetallic hollow nanostructures of electrocatalysts not only for water splitting but also for other catalytic reactions, as our synthetic strategy outlined here can be applied to the design of other shapes and facets of nickel and many other 3d transition metals.

METHODS AND MATERIALS

Materials: Nickel (II) chloride ($NiCl_2$, 98%, MERCK), Iridium (IV) chloride hydrate ($IrCl_4$, 99.9%, MERCK), oleylamine (technical grade, 70%, MERCK), ethanol (99.8%, MERCK), toluene (99%, Alfa Aesar), Hydrochloric acid (HCl, 37%, Alfa Aesar) were used without additional purification.

Synthesis of hexagonal NiIr nanostructures: 0.09 mmol of $IrCl_4$ and 0.12 mmol of $NiCl_2$ mixed with 24.3 mmol of oleylamine in a round-bottom flask. The flask was placed in a preheated oil bath at 100 ^oC and stirred for 30 min with flowing Ar gas, which was followed by heating the oil bath to 260 ^oC and maintaining the temperature for 30 min. After 30 min, the flask cooled to ambient temperature under Ar atmosphere. The solution was flushed with toluene and ethanol several times until the transparent supernatant was achieved. The obtained dark precipitates were dried overnight under vacuum.

Synthesis of the NiIr hollow nanoframes: The NiIr hexagonal nanostructures were re-dispersed in the mixed solution of ethanol, toluene, and HCl with a 1:1:1 volume ratio. The mixture was then placed in a preheated oil bath at 70 ^oC for 1 h. After being allowed to cool to ambient temperature, the solution flushed with ethanol three times. The resulting precipitates dried under vacuum.

Morphological, Structural and Elemental Characterization: Scanning transmission electron microscopy and energy-dispersive X-ray spectroscopy investigations were conducted using an FEI (Thermo Fisher Scientific) Titan 80–200 electron microscope that utilized a probe corrector (CEOS) and a HAADF detector.[70] To achieve "Z-contrast" conditions, a probe semi-angle of 25 mrad was used with the detector having a 65 mrad inner collection angle. For the EDX elemental mapping, Ir L and Ni K peaks were utilized. X-ray diffractions (XRD) were measured in D8 DISCOVER (Bruker) using a Cu Ka source and LYNXEYE_XE_T as the detector. X-ray photoelectron spectra (XPS) collected with Phi5000 VersaProbeII from ULVAC-Phi Inc. with Al Ka as the monochromatic (1.486 keV) used as a source. The powder samples were pressed into Indium foil fixed with clamps on a stainless steel sample holder. The core-level spectra recorded with a pass energy of 23.5 eV, 0.1 eV energy step, and a spot size of 200 µm. An electron flood gun and an Ar+ ion gun were used for charge compensation. The spectra were charge corrected by setting the binding energy of the main C1s component to 285 eV. Inductively coupled plasma mass spectrometry (ICP-MS, Agilent 7900) was used to measure the electrolyte after the durability.

Electrochemical Measurements. A typical three-electrode configuration with a reversible hydrogen electrode (RHE) serving as the reference electrode and a Pt mesh rod as the counter electrode used. A glassy carbon electrode (GC) (diameter: 5 mm, area: 0.196 cm^2) was the working electrode. The ink prepared by mixing 3.5 mg of catalysts with 0.7 mg of Vulcan X-72 in DI water (7.6 ml), Isopropanol (2.4 ml), and 5 % of Nafion (40 µl). The mixture was then sonicated for 30 min to form a homogeneous dispersion. Then, 10 µl of well-dispersed ink was mixed into the GC and dried naturally at ambient temperature. The catalyst's loading on the GC was 17.8 $\mu g \cdot cm^{-2}$. 0.5M of H_2SO_4 was used as the electrolyte. The cell purged with N_2 before starting the measurements. The cyclic voltammetry runs between +0.4 V and +1.4 V with a scan rate of 50 $mV \cdot s^{-1}$. Linear sweep voltammetry was recorded from +0.4 V to +1.7 V at a scan rate of 5 $mV \cdot s^{-1}$ with saturated O_2.

ASSOCIATED CONTENT

The Supporting Information is available free of charge at https://pubs.acs.org

- Additional information including: images showing the role of the metal precursors, TEM images, HAADF-STEM image with additional EDX composition maps, polarization curves of mass activity, Tafel plot.

AUTHOR INFORMATION

Corresponding Author

Meital Shviro- Institute of Energy and Climate Research, Electrochemical Process Engineering (IEK-14) Forschungszentrum Jülich GmbH, 52425 Jülich, Germany. https://orcid.org/0000-0002-9494-0233; E-mail: m.shviro@fz-juelich.de

Authors

Seongeun Park- Institute of Energy and Climate Research, Electrochemical Process Engineering (IEK-14) Forschungszentrum Jülich GmbH, 52425 Jülich, Germany.

Heinrich Hartmann- Central Institute for Engineering, Electronics and Analytics (ZEA-3) Forschungszentrum Jülich GmbH, 52425 Jülich, Germany. https://orcid.org/0000-0002-7244-495X

Astrid Besmehn- Central Institute for Engineering, Electronics and Analytics (ZEA-3) Forschungszentrum Jülich GmbH, 52425 Jülich, Germany. https://orcid.org/0000-0001-8045-9118

Joachim Mayer- ER-C 2, Forschungszentrum Jülich GmbH, 52425 Jülich, Germany, GFE, RWTH Aachen University, 52074 Aachen, Germany. https://orcid.org/0000-0003-3292-5342

Detlef Stolten- Institute of Energy and Climate Research, Techno-economic Systems Analysis (IEK-3) Forschungszentrum Jülich GmbH, 52425 Jülich, Germany, Chair for Fuel Cells, RWTH Aachen University, Germany. https://orcid.org/0000-0002-1671-3262

Marcelo Carmo- Institute of Energy and Climate Research, Electrochemical Process Engineering (IEK-14) Forschungszentrum Jülich GmbH, 52425 Jülich, Germany, Mechanical and Materials Engineering, Queen's University, Kingston, ON, K7L 3N6, Canada. https://orcid.org/0000-0002-0186-317X

Author Contributions

‡ S.P and M.S contributed equally to this work

Notes

The authors declare no competing financial interest.

ACKNOWLEDGMENTS

M.S thanks the Alexander von Humboldt Foundation for financial support.

References

(1) Carmo, M.; Fritz, D. L.; Mergel, J.; Stolten, D. A Comprehensive Review on PEM Water Electrolysis. *Int. J. Hydrogen Energy* **2013**, *38* (12), 4901–4934. https://doi.org/10.1016/j.ijhydene.2013.01.151.

(2) Babic, U.; Suermann, M.; Büchi, F. N.; Gubler, L.; Schmidt, T. J. Review-Identifying Critical Gaps for Polymer Electrolyte Water Electrolysis Development. *J. Electrochem. Soc.* **2017**, *164* (4), F387–F399. https://doi.org/10.3929/ETHZ-B-000190719.

(3) Nosheen, F.; Anwar, T.; Siddique, A.; Hussain, N. Noble Metal Based Alloy Nanoframes: Syntheses and Applications in Fuel Cells. *Frontiers in Chemistry*. Frontiers Media S.A. 2019. https://doi.org/10.3389/fchem.2019.00456.

(4) Wu, G.; Li, X.; Zhang, Z.; Dong, P.; Xu, M.; Peng, H.; Zeng, X.; Zhang, Y.; Liao, S. Design of Ultralong-Life Li-CO2 Batteries with IrO2 Nanoparticles Highly Dispersed on Nitrogen-Doped Carbon Nanotubes. *J. Mater. Chem. A* **2020**, *8* (7), 3763–3770. https://doi.org/10.1039/c9ta11028c.

(5) Fang, Y.; Xue, Y.; Hui, L.; Yu, H.; Li, Y. Graphdiyne@Janus Magnetite for Photocatalytic Nitrogen Fixation. *Angew. Chemie Int. Ed.* **2021**, *60* (6), 3170–3174. https://doi.org/10.1002/anie.202012357.

(6) Zhao, Y.; Vargas-Barbosa, N. M.; Strayer, M. E.; McCool, N. S.; Pandelia, M. E.; Saunders, T. P.; Swierk, J. R.; Callejas, J. F.; Jensen, L.; Mallouk, T. E. Understanding the Effect of Monomeric Iridium(III/IV) Aquo Complexes on the Photoelectrochemistry of IrOx· n H2O-Catalyzed Water-Splitting Systems. *J. Am. Chem. Soc.* **2015**, *137* (27), 8749–8757. https://doi.org/10.1021/jacs.5b03470.

(7) Audichon, T.; Napporn, T. W.; Canaff, C.; Morais, C.; Comminges, C.; Kokoh, K. B. IrO 2 Coated on RuO 2 as Efficient and Stable Electroactive Nanocatalysts for Electrochemical Water Splitting. *J. Phys. Chem. C* **2016**, *120* (5), 2562–2573. https://doi.org/10.1021/acs.jpcc.5b11868.

(8) Lee, Y.; Suntivich, J.; May, K. J.; Perry, E. E.; Shao-Horn, Y. Synthesis and Activities of Rutile IrO_2 and RuO_2 Nanoparticles for Oxygen Evolution in Acid and Alkaline Solutions. *J. Phys. Chem. Lett.* **2012**, *3* (3), 399–404. https://doi.org/10.1021/jz2016507.

(9) Li, G.; Li, S.; Ge, J.; Liu, C.; Xing, W. Discontinuously Covered IrO_2 –RuO_2 @Ru Electrocatalysts for the Oxygen Evolution Reaction: How High Activity and Long-Term Durability Can Be Simultaneously Realized in the Synergistic and Hybrid Nano-Structure. *J. Mater. Chem. A* **2017**, *5* (33), 17221–17229. https://doi.org/10.1039/C7TA05126C.

(10) Hodnik, N.; Jovanovič, P.; Pavlišič, A.; Jozinović, B.; Zorko, M.; Bele, M.; Šelih, V. S.; Šala, M.; Hočevar, S.; Gaberščček, M. New Insights into Corrosion of Ruthenium and Ruthenium Oxide Nanoparticles in Acidic Media. *J. Phys. Chem. C* **2015**, *119* (18), 10140–10147. https://doi.org/10.1021/acs.jpcc.5b01832.

(11) Jang, H.; Hieu, T. T.; Kim, S. H.; Lee, J. Reduction of Iridium Loading to the Minimum Level Required for Water Oxidation Electrocatalysis without Sacrificing the Electrochemical Stability. *J. Phys. Chem. C* **2019**, acs.jpcc.9b02819. https://doi.org/10.1021/acs.jpcc.9b02819.

(12) Lettenmeier, P.; Wang, L.; Golla-Schindler, U.; Gazdzicki, P.; Cañas, N. A.; Handl, M.; Hiesgen, R.; Hosseiny, S. S.; Gago, A. S.; Friedrich, K. A. Nanosized IrO x -Ir Catalyst with Relevant Activity for Anodes of Proton Exchange Membrane Electrolysis Produced by a Cost-Effective Procedure. *Angew. Chemie* **2016**, *128* (2), 752–756. https://doi.org/10.1002/ange.201507626.

(13) Li, G.; Li, K.; Yang, L.; Chang, J.; Ma, R.; Wu, Z.; Ge, J.; Liu, C.; Xing, W. Boosted Performance of Ir Species by Employing TiN as the Support toward Oxygen Evolution Reaction. *ACS Appl. Mater. Interfaces* **2018**, *10* (44), 38117–38124. https://doi.org/10.1021/acsami.8b14172.

(14) Park, S.-A.; Kim, K.-S.; Kim, Y.-T. Electrochemically Activated Iridium Oxide Black as Promising Electrocatalyst Having High Activity and Stability for Oxygen Evolution Reaction. *ACS Energy Lett.* **2018**, *3* (5), 1110–1115. https://doi.org/10.1021/acsenergylett.8b00368.

(15) Alia, S. M.; Rasimick, B.; Ngo, C.; Neyerlin, K. C.; Kocha, S. S.; Pylypenko, S.; Xu, H.; Pivovar, B. S. Activity and Durability of Iridium Nanoparticles in the Oxygen Evolution Reaction. *J. Electrochem. Soc.* **2016**, *163* (11), F3105–F3112. https://doi.org/10.1149/2.0151611jes.

(16) Li, G.; Li, S.; Xiao, M.; Ge, J.; Liu, C.; Xing, W. Nanoporous IrO 2 Catalyst with Enhanced Activity and Durability for Water Oxidation Owing to Its Micro/Mesoporous Structure. *Nanoscale* **2017**, *9* (27), 9291–9298. https://doi.org/10.1039/C7NR02899G.

(17) Ahmed, J.; Mao, Y. Ultrafine Iridium Oxide Nanorods Synthesized by Molten Salt Method toward Electrocatalytic Oxygen and Hydrogen Evolution Reactions. *Electrochim. Acta* **2016**, *212*, 686–693. https://doi.org/10.1016/J.ELECTACTA.2016.06.122.

(18) Fu, L.; Yang, F.; Cheng, G.; Luo, W. Ultrathin Ir Nanowires as High-Performance Electrocatalysts for Efficient Water Splitting in Acidic Media. *Nanoscale* **2018**, *10* (4), 1892–1897. https://doi.org/10.1039/C7NR09377B.

(19) Oh, H.-S.; Nong, H. N.; Reier, T.; Gliech, M.; Strasser, P. Oxide-Supported Ir Nanodendrites with High Activity and Durability for the Oxygen Evolution Reaction in Acid PEM Water Electrolyzers. *Chem. Sci.* **2015**, *6* (6), 3321–3328. https://doi.org/10.1039/C5SC00518C.

(20) Alia, S. M.; Shulda, S.; Ngo, C.; Pylypenko, S.; Pivovar, B. S. Iridium-Based Nanowires as Highly Active, Oxygen Evolution Reaction Electrocatalysts. *ACS Catal.* **2018**, *8* (3), 2111–2120. https://doi.org/10.1021/acscatal.7b03787.

(21) Kwon, T.; Jun, M.; Joo, J.; Lee, K. Nanoscale Hetero-Interfaces between Metals and Metal Compounds for Electrocatalytic Applications. *J. Mater. Chem. A* **2019**, *7* (10), 5090–5110. https://doi.org/10.1039/C8TA09494B.

(22) McCrory, C. C. L.; Jung, S.; Ferrer, I. M.; Chatman, S. M.; Peters, J. C.; Jaramillo, T. F. Benchmarking Hydrogen Evolving Reaction and Oxygen Evolving Reaction Electrocatalysts for Solar Water Splitting Devices. *J. Am. Chem. Soc.* **2015**, *137* (13), 4347–4357. https://doi.org/10.1021/ja510442p.

(23) Suen, N.-T.; Hung, S.-F.; Quan, Q.; Zhang, N.; Xu, Y.-J.; Chen, H. M. Electrocatalysis for the Oxygen Evolution Reaction: Recent Development and Future Perspectives. *Chem. Soc. Rev.* **2017**, *46* (2), 337–365. https://doi.org/10.1039/C6CS00328A.

(24) Xia, Z.; Guo, S. Strain Engineering of Metal-Based Nanomaterials for Energy Electrocatalysis. *Chem. Soc. Rev.* **2019**. https://doi.org/10.1039/C8CS00846A.

(25) Park, J.; Kwon, T.; Kim, J.; Jin, H.; Kim, H. Y.; Kim, B.; Joo, S. H.; Lee, K. Hollow Nanoparticles as Emerging Electrocatalysts for Renewable Energy Conversion Reactions. *Chem. Soc. Rev.* **2018**, *47* (22), 8173–8202. https://doi.org/10.1039/C8CS00336J.

(26) Shviro, M.; Polani, S.; Zitoun, D. Hollow Octahedral and Cuboctahedral Nanocrystals of Ternary Pt-Ni-Au Alloys. *Nanoscale* **2015**, *7* (32), 13521–13529. https://doi.org/10.1039/C5NR03522H.

(27) Kwon, T.; Jun, M.; Kim, H. Y.; Oh, A.; Park, J.; Baik, H.; Joo, S. H.; Lee, K. Vertex-Reinforced PtCuCo Ternary Nanoframes as Efficient and Stable Electrocatalysts for the Oxygen Reduction Reaction and the Methanol Oxidation Reaction. *Adv. Funct. Mater.* **2018**, *28* (13), 1706440. https://doi.org/10.1002/adfm.201706440.

(28) Kwon, T.; Hwang, H.; Sa, Y. J.; Park, J.; Baik, H.; Joo, S. H.; Lee, K. Cobalt Assisted Synthesis of IrCu Hollow Octahedral Nanocages as Highly Active Electrocatalysts toward Oxygen Evolution Reaction. *Adv. Funct. Mater.* **2017**, *27* (7), 1604688. https://doi.org/10.1002/adfm.201604688.

(29) Park, J.; Kanti Kabiraz, M.; Kwon, H.; Park, S.; Baik, H.; Choi, S.-I.; Lee, K. Radially Phase Segregated PtCu@PtCuNi Dendrite@Frame Nanocatalyst for the Oxygen Reduction Reaction. *ACS Nano* **2017**, *11* (11), 10844–10851. https://doi.org/10.1021/acsnano.7b04097.

(30) Pei, J.; Mao, J.; Liang, X.; Chen, C.; Peng, Q.; Wang, D.; Li, Y. Ir–Cu Nanoframes: One-Pot Synthesis and Efficient Electrocatalysts for Oxygen Evolution Reaction. *Chem. Commun.* **2016**, *52* (19), 3793–3796. https://doi.org/10.1039/C6CC00552G.

(31) Wang, C.; Sui, Y.; Xiao, G.; Yang, X.; Wei, Y.; Zou, G.; Zou, B. Synthesis of Cu–Ir Nanocages with Enhanced Electrocatalytic Activity for the Oxygen Evolution Reaction. *J. Mater. Chem. A* **2015**, *3* (39), 19669–19673. https://doi.org/10.1039/C5TA05384F.

(32) Sun, X.; Kim, J.; Gilroy, K. D.; Liu, J.; König, T. A. F.; Qin, D. Gold-Based Cubic Nanoboxes with Well-Defined Openings at the Corners and Ultrathin Walls Less Than Two Nanometers Thick. *ACS Nano* **2016**, *10* (8), 8019–8025. https://doi.org/10.1021/acsnano.6b04084.

(33) Hong, J. W.; Kang, S. W.; Choi, B.-S.; Kim, D.; Lee, S. B.; Han, S. W. Controlled Synthesis of Pd–Pt Alloy Hollow Nanostructures with Enhanced Catalytic Activities for Oxygen Reduction. *ACS Nano* **2012**, *6* (3), 2410–2419. https://doi.org/10.1021/nn2046828.

(34) Han, L.; Wang, P.; Liu, H.; Tan, Q.; Yang, J. Balancing the Galvanic Replacement and Reduction Kinetics for the General Formation of Bimetallic CuM (M = Ru, Rh, Pd, Os, Ir, and Pt) Hollow Nanostructures. *J. Mater. Chem. A* **2016**, *4* (47), 18354–18365. https://doi.org/10.1039/C6TA08465F.

(35) Park, J.; Sa, Y. J.; Baik, H.; Kwon, T.; Joo, S. H.; Lee, K. Iridium-Based Multimetallic Nanoframe@Nanoframe Structure: An Efficient and Robust Electrocatalyst toward Oxygen Evolution Reaction. *ACS Nano* **2017**, *11* (6), 5500–5509. https://doi.org/10.1021/acsnano.7b00233.

(36) Fu, L.; Cheng, G.; Luo, W. Colloidal Synthesis of Monodisperse Trimetallic IrNiFe Nanoparticles as Highly Active Bifunctional Electrocatalysts for Acidic Overall Water Splitting. *J. Mater. Chem. A* **2017**, *5* (47), 24836–24841. https://doi.org/10.1039/C7TA08982A.

(37) Fu, L.; Cai, P.; Cheng, G.; Luo, W. Colloidal Synthesis of Iridium-Iron Nanoparticles for Electrocatalytic Oxygen Evolution. *Sustain. Energy Fuels* **2017**, *1* (5), 1199–1203. https://doi.org/10.1039/C7SE00113D.

(38) Lima, F. H. B.; Zhang, J.; Shao, M. H.; Sasaki, K.; Vukmirovic, M. B.; Ticianelli, E. A.; Adzic, R. R. Catalytic Activity-d-Band Center Correlation for the O 2 Reduction Reaction on Platinum in Alkaline Solutions. **2007**. https://doi.org/10.1021/jp065181r.

(39) Xue, Y.; Huang, B.; Yi, Y.; Guo, Y.; Zuo, Z.; Li, Y.; Jia, Z.; Liu, H.; Li, Y. Anchoring Zero Valence Single Atoms of Nickel and Iron on Graphdiyne for Hydrogen Evolution. *Nat. Commun.* **2018**, *9* (1), 1–10. https://doi.org/10.1038/s41467-018-03896-4.

(40) Lim, J.; Yang, S.; Kim, C.; Roh, C.-W.; Kwon, Y.; Kim, Y.-T.; Lee, H. Shaped Ir–Ni Bimetallic Nanoparticles for Minimizing Ir Utilization in Oxygen Evolution Reaction. *Chem. Commun.* **2016**, *52* (32), 5641–5644. https://doi.org/10.1039/C6CC00053C.

(41) Wang, L. L.; Johnson, D. D. Predicted Trends of Core-Shell Preferences for 132 Late Transition-Metal Binary-Alloy Nanoparticles. *J. Am. Chem. Soc.* **2009**, *131* (39), 14023–14029. https://doi.org/10.1021/ja903247x.

(42) Nong, H. N.; Reier, T.; Oh, H.-S.; Gliech, M.; Paciok, P.; Ha, T.; Vu, T.; Teschner, D.; Heggen, M.; Petkov, V.; Schlögl, R.; Jones, T.; Strasser, P. A Unique Oxygen Ligand Environment Facilitates Water Oxidation in Hole-Doped IrNiOx Core–Shell Electrocatalysts. **1929**. https://doi.org/10.1038/s41929-018-0153-y.

(43) Reier, T.; Pawolek, Z.; Cherevko, S.; Bruns, M.; Jones, T.; Teschner, D.; Selve, S.; Bergmann, A.; Nong, H. N.; Schlögl, R.; Mayrhofer, K. J. J.; Strasser, P. Molecular Insight in Structure and Activity of Highly Efficient, Low-Ir Ir–Ni Oxide Catalysts for Electrochemical Water Splitting (OER). *J. Am. Chem. Soc.* **2015**, *137* (40), 13031–13040. https://doi.org/10.1021/jacs.5b07788.

(44) Back, S.; Yeom, M. S.; Jung, Y. Active Sites of Au and Ag Nanoparticle Catalysts for CO 2 Electroreduction to CO. **2015**. https://doi.org/10.1021/acscatal.5b00462.

(45) Zalitis, C. M.; Kucernak, A. R.; Sharman, J.; Wright, E. Design Principles for Platinum Nanoparticles Catalysing Electrochemical Hydrogen Evolution and Oxidation Reactions: Edges Are Much More Active than Facets. *J. Mater. Chem. A* **2017**, *5* (44), 23328–23338. https://doi.org/10.1039/c7ta05543a.

(46) Xia, X.; Figueroa-Cosme, L.; Tao, J.; Peng, H. C.; Niu, G.; Zhu, Y.; Xia, Y. Facile Synthesis of Iridium Nanocrystals with Well-Controlled Facets Using Seed-Mediated Growth. *J. Am. Chem. Soc.* **2014**, *136* (31), 10878–10881. https://doi.org/10.1021/ja505716v.

(47) Bang, S.; Yoon, D.; Kim, J.; Baik, H.; Yang, H.; Lee, K. Formation of Double Layer Hollow Nanostars of Pd/CuIr by Utilizing a Kirkendall Effect and a Facile Cu Atom Movement along Twinning Boundaries and Their Usage as Efficient Water Splitting Catalysts. *CrystEngComm* **2015**, *17* (22), 4084–4088. https://doi.org/10.1039/C5CE00538H.

(48) Pan, Y.; Liu, Y.; Zhao, J.; Yang, K.; Liang, J.; Liu, D.; Hu, W.; Liu, D.; Liu, Y.; Liu, C. Monodispersed Nickel Phosphide Nanocrystals with Different Phases: Synthesis, Characterization and Electrocatalytic Properties for Hydrogen Evolution. *J. Mater. Chem. A* **2015**, *3* (4), 1656–1665. https://doi.org/10.1039/C4TA04867A.

(49) Biesinger, M. C.; Payne, B. P.; Lau, L. W. M.; Gerson, A.; Smart, R. S. C. X-Ray Photoelectron Spectroscopic Chemical State Quantification of Mixed Nickel Metal, Oxide and Hydroxide Systems. *Surf. Interface Anal.* **2009**, *41* (4), 324–332. https://doi.org/10.1002/sia.3026.

(50) Biesinger, M. C.; Payne, B. P.; Grosvenor, A. P.; Lau, L. W. M.; Gerson, A. R.; Smart, R. S. C. Resolving Surface Chemical States in XPS Analysis of First Row Transition Metals, Oxides and Hydroxides: Cr, Mn, Fe, Co and Ni. *Appl. Surf. Sci.* **2011**, *257* (7), 2717–2730. https://doi.org/10.1016/j.apsusc.2010.10.051.

(51) Mcintyre, N. S.; Cook, M. G. X-Ray Photoelectron Studies on Some Oxides and Hydroxides of Cobalt, Nickel, and Copper. *Anal. Chem.* **1975**, *47* (13), 2208–2213. https://doi.org/10.1021/ac60363a034.

(52) Freakley, S. J.; Ruiz-Esquius, J.; Morgan, D. J. The X-Ray Photoelectron Spectra of Ir, IrO2 and IrCl3 Revisited. *Surf. Interface Anal.* **2017**, *49* (8), 794–799. https://doi.org/10.1002/sia.6225.

(53) Alia, S. M.; Shulda, S.; Ngo, C.; Pylypenko, S.; Pivovar, B. S. Iridium-Based Nanowires as Highly Active, Oxygen Evolution Reaction Electrocatalysts. *ACS Catal.* **2018**, *8* (3), 2111–2120. https://doi.org/10.1021/acscatal.7b03787.

(54) Ruiz Esquius, J.; Morgan, D. J.; Spanos, I.; Hewes, D. G.; Freakley, S. J.; Hutchings, G. J. Effect of Base on the Facile Hydrothermal Preparation of Highly Active IrO x Oxygen Evolution Catalysts. *ACS Appl. Energy Mater.* **2020**, *3* (1), 800–809. https://doi.org/10.1021/acsaem.9b01642.

(55) Godínez-Salomón, F.; Albiter, L.; Alia, S. M.; Pivovar, B. S.; Camacho-Forero, L. E.; Balbuena, P. B.; Mendoza-Cruz, R.; Arellano-Jimenez, M. J.; Rhodes, C. P. Self-Supported Hydrous Iridium–Nickel Oxide Two-Dimensional Nanoframes for High Activity Oxygen Evolution Electrocatalysts. *ACS Catal.* **2018**, *8* (11), 10498–10520. https://doi.org/10.1021/acscatal.8b02171.

(56) Nong, H. N.; Gan, L.; Willinger, E.; Teschner, D.; Strasser, P. IrOx Core-Shell Nanocatalysts for Cost- and Energy-Efficient Electrochemical Water Splitting. *Chem. Sci.* **2014**, *5* (8), 2955–2963. https://doi.org/10.1039/c4sc01065e.

(57) Rakousky, C.; Shviro, M.; Carmo, M.; Stolten, D. Iridium Nanoparticles for the Oxygen Evolution Reaction: Correlation of Structure and Activity of Benchmark Catalyst Systems. *Electrochim. Acta* **2019**, *302*, 472–477. https://doi.org/10.1016/j.electacta.2018.11.141.

(58) Ren, M.; Chen, J.; Li, Y.; Zhang, H.; Zou, Z.; Li, X.; Yang, H. Lattice Contracted Pd-Hollow Nanocrystals: Synthesis, Structure and Electrocatalysis for Formic Acid Oxidation. *J. Power Sources* **2014**, *246*, 32–38. https://doi.org/10.1016/j.jpowsour.2013.07.067.

(59) Wang, X.; Figueroa-Cosme, L.; Yang, X.; Luo, M.; Liu, J.; Xie, Z.; Xia, Y. Pt-Based Icosahedral

Nanocages: Using a Combination of {111} Facets, Twin Defects, and Ultrathin Walls to Greatly Enhance Their Activity toward Oxygen Reduction. **2016**. https://doi.org/10.1021/acs.nanolett.5b05140.

(60) Sheng, D.; He, D.; Wang, J.; Lin, Y.; Yin, P.; Hong, X.; Wu, Y.; Li, Y. Ultrathin Icosahedral Pt-Enriched Nanocage with Excellent Oxygen Reduction Reaction Activity. **2016**. https://doi.org/10.1021/jacs.5b12530.

(61) Huang, K.; Hou, J.; Zhang, Q.; Ou, G.; Ning, D.; Hussain, N.; Xu, Y.; Ge, B.; Liu, K.; Wu, H. Ultrathin Two-Dimensional Metals with Fully Exposed (111) Facets. *Chem. Commun.* **2017**, *54* (2), 160–163. https://doi.org/10.1039/c7cc07923k.

(62) Beermann, V.; Gocyla, M.; Willinger, E.; Rudi, S.; Heggen, M.; Dunin-Borkowski, R. E.; Willinger, M. G.; Strasser, P. Rh-Doped Pt-Ni Octahedral Nanoparticles: Understanding the Correlation between Elemental Distribution, Oxygen Reduction Reaction, and Shape Stability. *Nano Lett.* **2016**, *16* (3), 1719–1725. https://doi.org/10.1021/acs.nanolett.5b04636.

(63) Abbott, D. F.; Lebedev, D.; Waltar, K.; Povia, M.; Nachtegaal, M.; Fabbri, E.; Copéret, C.; Schmidt, T. J. Iridium Oxide for the Oxygen Evolution Reaction: Correlation between Particle Size, Morphology, and the Surface Hydroxo Layer from Operando XAS. *Chem. Mater.* **2016**, *28* (18), 6591–6604. https://doi.org/10.1021/acs.chemmater.6b02625.

(64) Antolini, E. Iridium As Catalyst and Cocatalyst for Oxygen Evolution/Reduction in Acidic Polymer Electrolyte Membrane Electrolyzers and Fuel Cells. **2014**. https://doi.org/10.1021/cs4011875.

(65) Li, G.; Li, S.; Ge, J.; Liu, C.; Xing, W. Discontinuously Covered IrO2-RuO2@Ru Electrocatalysts for the Oxygen Evolution Reaction: How High Activity and Long-Term Durability Can Be Simultaneously Realized in the Synergistic and Hybrid Nano-Structure. *J. Mater. Chem. A* **2017**, *5* (33), 17221–17229. https://doi.org/10.1039/c7ta05126c.

(66) Hartig-Weiss, A.; Miller, M.; Beyer, H.; Schmitt, A.; Siebel, A.; Freiberg, A. T. S.; Gasteiger, H. A.; El-Sayed, H. A. Iridium Oxide Catalyst Supported on Antimony-Doped Tin Oxide for High Oxygen Evolution Reaction Activity in Acidic Media. *ACS Appl. Nano Mater.* **2020**. https://doi.org/10.1021/acsanm.9b02230.

(67) Huang, R.; Wen, Y. H.; Zhu, Z. Z.; Sun, S. G. Atomic-Scale Insights into Structural and Thermodynamic Stability of Pd-Ni Bimetallic Nanoparticles. *Phys. Chem. Chem. Phys.* **2016**, *18* (14), 9847–9854. https://doi.org/10.1039/c5cp07555f.

(68) Sharma, G.; Kumar, A.; Sharma, S.; Naushad, M.; Prakash Dwivedi, R.; ALOthman, Z. A.; Mola, G. T. Novel Development of Nanoparticles to Bimetallic Nanoparticles and Their Composites: A Review. *Journal of King Saud University - Science*. Elsevier B.V. April 1, 2019, pp 257–269. https://doi.org/10.1016/j.jksus.2017.06.012.

(69) Loza, K.; Heggen, M.; Epple, M. Synthesis, Structure, Properties, and Applications of Bimetallic Nanoparticles of Noble Metals. *Adv. Funct. Mater.* **2020**, *30* (21), 1909260. https://doi.org/10.1002/adfm.201909260.

(70) Kovács, A.; Schierholz, R.; Tillmann, K. FEI Titan G2 80-200 CREWLEY. *J. large-scale Res. Facil. JLSRF* **2016**, *2* (0), A43. https://doi.org/10.17815/jlsrf-2-68.